Preferential concentration of noninertial buoyant particles in the ocean mixed layer under free convection

Tomás Chor
Department of Atmospheric and Oceanic Sciences, University of California, Los Angeles, Los Angeles, California 90095, USA

Di Yang
Department of Mechanical Engineering, Cullen College of Engineering, University of Houston, Houston, Texas 77204-4006, USA

Charles Meneveau
Department of Mechanical Engineering, Johns Hopkins University, Baltimore, Maryland 21218, USA

Marcelo Chamecki*
Department of Atmospheric and Oceanic Sciences, University of California, Los Angeles, Los Angeles, California 90095, USA

(Received 27 March 2018; published 28 June 2018)

In this work we investigate buoyant particle dynamics in the ocean mixed layer (OML) under a purely convective regime. We focus on noninertial particles that are lighter than the surrounding seawater (thus, buoyant), which is a useful configuration when representing oil, microplastic debris, and other buoyant materials that do not necessarily exhibit strong inertial effects. Our main goal is to understand and describe the physical mechanisms that control the buoyant particles' surface concentration under such conditions, specifically the preferential concentration effects that arise independently of inertia (rather than the well-known centrifuging mechanism for heavy particles). In our investigation we use large-eddy simulation to model the particle dispersion in the OML in which the evolution of the particle field is simulated using an Eulerian approach. We find that in addition to the preferential concentration effect that clusters particles into convergence regions on the surface (which is a well-known and straightforward effect on free surfaces), there is a secondary effect for highly buoyant particles that drives them into vorticity-dominated regions. We explain this effect as the advection of buoyant particles by persistent vortices in the flow, which turns out to be the dominating mechanism controlling the surface particle distribution. Highly buoyant particles are trapped in the interior of the vortices (at the surface), which favors clustering in vorticity-dominated regions, while for particles with low buoyancy this effect is negligible.

DOI: 10.1103/PhysRevFluids.3.064501

I. INTRODUCTION

The near-surface portion of the ocean, namely, the ocean mixed layer (OML), is strongly influenced by the dynamic processes induced by the atmospheric forcing and is generally weakly stratified and well mixed [1]. It is also usually an important destination for positively buoyant particles, which tend to rise to the surface, often becoming trapped in it. This makes the evolution of buoyant particles in the

*Corresponding author: chamecki@ucla.edu

OML an important subject, with various relevant applications such as transport of ocean debris [2–4], oil spills [5,6], and bubble dynamics [7]. Considering, as an example, the case of oil spills, a thorough understanding of the basic physics and underlying dynamics is vital, since the fate of oil plumes in the ocean surface must be often rapidly predicted using physics-based models. The present work focuses on the dynamics of buoyant particles in the OML under purely convective conditions, with an emphasis on small-scale three-dimensional turbulence in the absence of mesoscale and submesoscale features. Despite its importance and despite there have been several recent investigations focusing on small-scale turbulence effects [4–6,8–11] and submesoscale phenomena [12–14], the evolution of buoyant particles in the OML under such conditions has not been addressed in detail to date.

In order to illustrate the precise scope of this work, consider the approximate particle velocity equation [15,16]

$$\boldsymbol{v} = \boldsymbol{u} + w_r \boldsymbol{e}_3 + \frac{w_r}{g}\frac{d\boldsymbol{v}}{dt}, \tag{1}$$

where $\boldsymbol{v}$ is the total particle velocity, $\boldsymbol{u}$ is the flow velocity, w_r is the particle terminal rise velocity (we assume $w_r > 0$, i.e., the particles are less dense than the carrier fluid), g is the gravitational acceleration, t is the time, and $\boldsymbol{e}_3$ is the unit vector in the vertical upward-pointing direction (more details on the approximations that lead to this simplified equation are discussed in Sec. III). The first two terms on the right-hand side are the particle advection by the flow and the terminal rise velocity that comes from the balance between buoyancy and drag forces. The third term corresponds to inertial effects and can generally be approximated by $w_r g^{-1} D\boldsymbol{u}/Dt$ after an expansion in particle timescale [15,16], where $D(\cdot)/Dt$ is the material derivative. We are interested in flows for which the third term on the right-hand side of Eq. (1) is small compared to w_r, i.e., cases in which the condition $g^{-1}d\boldsymbol{v}/dt \ll 1$ is satisfied. These are particles whose velocity is dominated by flow advection and buoyancy effects, but with comparably weak inertial effects. In the OML this often includes oil droplets, microplastic debris, bubbles, etc.

The omission of the inertial term allows us to focus our attention on a form of preferential concentration that arises independently of particle inertia. This effect is illustrated in the case of a purely convective flow represented in Figs. 1(a)–1(c), which shows the particle concentration field C obtained via large-eddy simulation (LES) using an Eulerian approach (whose details will be given in Sec. III). In all cases displayed we use noninertial particles with increasing buoyancy from Fig. 1(a) to Fig. 1(c). It is clear from the figures that there is preferential concentration of particles in zones of horizontal convergence, shown in Fig. 1(d) by regions of negative normalized divergence D, defined as

$$D = \frac{1}{\langle |\boldsymbol{S}| \rangle_{\mathrm{vt}}} \left(\frac{\partial u}{\partial x} + \frac{\partial v}{\partial y} \right) \Bigg|_{z=0}, \tag{2}$$

while there is significantly low concentration in divergence regions where D is positive. In Eq. (2), $\boldsymbol{S} = \frac{1}{2}[\nabla \boldsymbol{u} + (\nabla \boldsymbol{u})^T]$ is the three-dimensional strain rate tensor and $\langle \cdot \rangle_{\mathrm{vt}}$ denotes a Reynolds average which is approximated for practical purposes as a volume and time average. This particular effect (referred to here as the primary preferential concentration effect) is expected and qualitatively simple to understand as the result of downwelling plumes. Particles with very low or no buoyancy are easily submerged in the surface convergence regions due to downwelling and thus can resurface in the divergent upwelling regions. This tends to homogenize the surface particle distribution since this process effectively provides a communication channel between areas of convergence and divergence at the surface. Particles with higher buoyancy are not as easily submerged and thus do not experience as effectively this communication between downwelling and upwelling zones. Therefore, the main effect of the flow on particles with high buoyancy is to expel them from the divergence zones and into the convergence zones, where they tend to remain "trapped" for the most part while more particles are collected into the same convergent region.

There is an additional preferential concentration effect (referred to here as secondary) which can be noted by analyzing the horizontal scales of the surface particle distributions in Fig. 1. Notice

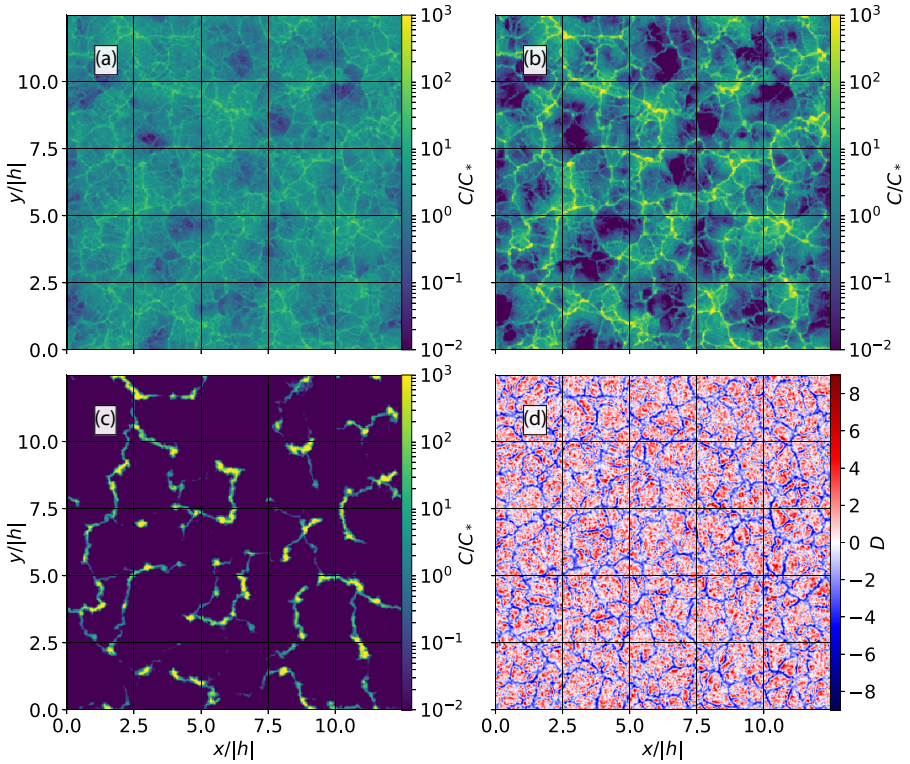

FIG. 1. Normalized surface concentrations for particles (a) C0.19, (b) C0.44, and (c) C1.21 (in order of increasing buoyancy) and (d) horizontal divergence D at the surface. Here h is the OML depth and all panels correspond to the same instant in time; C_* is a concentration scale, whose details will be given in Sec. III.

that, because of the mechanism just described above, particles in Figs. 1(a) and 1(b) are arranged following the convective cells shown in Fig. 1(d), making the horizontal scales of the distributions seen in Figs. 1(a) and 1(b) and Fig. 1(d) similar. Conversely, the highly buoyant particles in Fig. 1(c) are organized in a significantly larger horizontal scale than both the convective cells and the particles with lower buoyancy, being mostly concentrated in much smaller regions. This is exactly the secondary preferential concentration effect, which is not as straightforward to explain as the primary one and which becomes evident only for particles with "high buoyancy" and after being advected by the flow after a "certain time" (the precise definition of these terms will become clear in Sec. IV B). We later argue that this is the effect of small-scale vertical vortices, which tend to collect particles in convergent regions of high vorticity. Since inertial effects would introduce a similar preferential concentration behavior (centrifuging [17]), inertia was not considered in order to fully isolate this effect. Note that for both preferential concentration effects, the resulting behavior is for tracerlike particles to be mostly homogenized in the OML, while floaterlike particles are clustered together in isolated regions on the surface.

To date, most studies that dealt with particles in the OML considered either neutrally buoyant particles, which we refer to as tracers, or purely two-dimensional (2D) surface-moving particles, which we refer to as floaters (e.g., Ref. [10]). Although many scalars of interest may be approximated by one of those limiting cases, there are many instances for which such an approximation is not possible. In fact, earlier works that explored the range in between tracers and floaters showed that particle distributions in the OML strongly depend on the particle's terminal rise velocity [4–6,11]. The precise dependence, however, appears to have to be investigated on a case-by-case approach for different flow configurations given that the dominating flow structures depend on the forcing

mechanisms that drive the flow (e.g., convective plumes produce significantly different patterns from Langmuir cells, which themselves are different from patterns in wind-shear-driven flows). In this work we focus on particle dispersion in a convection-driven OML, which is a regime that has been somewhat unexplored by recent literature (an exception is the work by Mensa *et al.* [10]).

We proceed to define the goals of this work. The first one is to quantify both the primary and secondary preferential concentrations under a free-convection regime for particles with different buoyancies. The second objective is to use these quantifications to understand and describe the mechanisms that lead to the secondary preferential concentration of particles (the primary preferential concentration is fairly straightforward to understand, so there is no need to focus on it).

The paper is organized as follows. In Sec. II we review the basic physics that govern the dispersion on buoyant particles in the OML. In Sec. III we describe the numerical model used to obtain our results. In Sec. IV the results are presented and discussed in detail. Flow characteristics are described in Sec. IV A and the mechanism responsible for the secondary preferential concentration effect is described in Sec. IV B. We present a summary in Sec. V.

II. ANALYTIC CONSIDERATIONS

In this section we briefly review some basic physical properties and analytical results that will aid us in the following sections. Throughout the paper we adopt the usual notation that a variable A can be separated into a Reynolds average $\langle A \rangle$ and a turbulent fluctuation A'. For practical purposes $\langle \cdot \rangle$ is calculated as a horizontal and time average unless otherwise noted with a subscript and a comment. As mentioned, we neglect the inertial effects on the particles, which is justified in Sec. III B. Thus, we can rewrite Eq. (1) without the inertial term as

$$\boldsymbol{v} = \boldsymbol{u} + w_r \boldsymbol{e}_3. \tag{3}$$

Both Eqs. (1) and (3) are the result of several other assumptions about the nature of the particles' interaction with the flow. First, we assume that the particle volume fraction is always small enough to make particle feedback on the flow negligible, but large enough to make an Eulerian approach valid [15]. Furthermore, we consider that the size of the particles is smaller than the Kolmogorov scales of the flow, which allows us to neglect several effects that would be costly to model [16]. We use x and y for horizontal planes and set $z = 0$ at the ocean surface with z decreasing to negative values below the surface. Given these assumptions, we neglect effects such as Brownian motion, history force, thermophoresis, subgrid-scale (SGS) fluid stress force, Faxen effects, lift force, and virtual-mass effects, similar to simplifications made in several other studies [7,16]. Thus, the only effects that we assume to be important and that are included in Eq. (3) are gravity, drag, and buoyancy, which are accounted for by the parameter w_r.

Now we consider the surface particle concentrations in Fig. 1. Since both the primary and secondary preferential concentration effects happen even when the initial condition is a uniform concentration in the OML, we can understand them as the effect of a divergence introduced in the particle velocity field, given that preferential concentration of a scalar that is initially well mixed only happens when its velocity field is divergent [10]. Given that the flow is solenoidal at all points and that the terminal rise velocity is zero at $z = 0$ [which can be taken into account by using the Heaviside step function $H(-z)$ along with w_r], one can obtain a measure of the divergence of the particle velocity field by applying the divergence operator on Eq. (3) as

$$\nabla \cdot \boldsymbol{v} = \nabla \cdot \boldsymbol{u} + w_r \frac{\partial}{\partial z} H(-z) = w_r \delta(-z), \tag{4}$$

where $\delta(-z)$ is the Dirac delta function [note that $\delta(-z)$ has units of m^{-1}]. It is clear from Eq. (4) that passive tracers follow a three-dimensional nondivergent velocity field, while for any other case the velocity field is divergent at the surface (proportionally to w_r). At the other extreme is the floater regime, which can be understood as $w_r \to \infty$. Although not directly inferred from Eq. (4), it is possible to show (using the conservation of mass of a buoyant scalar) that in this case the divergence

of the particles' velocity field is proportional to the two-dimensional horizontal divergence at the surface (since all the mass concentrates at the surface). Thus, we can regard w_r as a parameter characterizing the continuous range between the purely solenoidal 3D and the divergent 2D particle velocity field cases.

At this point, it is important to make a clear distinction between the preferential concentration mechanism identified here and the well-known case for inertial particles [8,17,18]. In both cases, the preferential concentration arises from a divergence in the particle velocity field. However, while in the case for inertial particles this divergence source arises from an inertial term in $\boldsymbol{v}$, in our case it comes solely from the discontinuity in the terminal rise velocity w_r at the free surface. Thus, the mechanism in our case is not connected to any inertial effects and the only necessary conditions for it to take place are that the particles must have buoyancy, the flow must have a free surface where the particle terminal rise velocity is zero, and this surface should have a free-slip condition.

Based on the fact that w_r dictates the divergence of the particle velocity field, we introduce the floatability parameter β, which is an estimate of the physical balance between w_r (a tendency of particles to rise to the surface) and w_* (the eddies' tendency to submerge particles). Here β is defined as

$$\beta = \frac{w_r}{w_*}, \tag{5}$$

where w_* is the Deardorff convective velocity [19]

$$w_* = (g\alpha\langle w'\theta'\rangle_s|h|)^{1/3} = (B_0|h|)^{1/3}, \tag{6}$$

α is the thermal expansion coefficient, w' is the vertical velocity fluctuation, θ' is the temperature fluctuation, h is the OML depth, B_0 is the outward buoyancy flux at the surface, and $\langle\cdot\rangle_s$ denotes a Reynolds average at the surface (approximated for practical purposes as a horizontal and time average). Throughout this work we focus on interpreting the results in terms of β, rather than w_r, in order to render the results more general and scalable among different free-convection conditions.

III. SIMULATIONS

A. The LES description

We use LES to numerically investigate the phenomena introduced in the preceding sections with a code that has been applied successfully in other works [5,6]. The main equations are the filtered three-dimensional incompressible Navier-Stokes equations with the Lilly-Smagorinsky eddy viscosity model for the SGS closure [20,21]. In our equations Coriolis effects and particle feedbacks on the flow are excluded (see Sec. III B). The Smagorinsky coefficient is determined dynamically during the simulation using the Lagrangian-averaged scale-dependent dynamic SGS model [22]. The seawater density is assumed to have a linear dependence on the temperature θ and the SGS heat flux closure is achieved by specifying a turbulent SGS Prandtl number (here taken as $\mathrm{Pr}_{\mathrm{SGS}} = 0.4$). For more details about the equations and the code used, the reader is directed to Sec. 2 of Ref. [16], keeping in mind the fact that in this work we ignore the Stokes vortex force, the Coriolis acceleration, and particle-induced forces on the flow (i.e., the particle field is transported passively). The particle mass concentration is described by an Eulerian scalar field whose evolution is governed by (here a tilde denotes a grid-resolved variable)

$$\frac{\partial\tilde{C}}{\partial t} + \boldsymbol{\nabla}\cdot(\tilde{\boldsymbol{v}}\tilde{C}) = -\boldsymbol{\nabla}\cdot\boldsymbol{\pi}_C, \tag{7}$$

where $\boldsymbol{\pi}_C = \widetilde{\boldsymbol{u}C} - \tilde{\boldsymbol{u}}\tilde{C}$ is the SGS flux of particle concentration, molecular diffusion is neglected owing to the dominant effects of turbulence at the scales of the LES, and $\tilde{\boldsymbol{v}}$ is the resolved velocity of the particle field, given by

$$\tilde{\boldsymbol{v}} = \tilde{\boldsymbol{u}} + w_r\boldsymbol{e}_3, \tag{8}$$

which is the grid-filtered version of Eq. (3).

TABLE I. Simulation parameters used in this work. The eddy turnover time is defined as $T_* = |h|/w_*$, where the convective velocity w_* is defined in Eq. (6).

Name (notation)	Values
dimensions $L_x \times L_y \times L_z$	$1000 \times 1000 \times 120$ m^3
grid points $N_x \times N_y \times N_z$	$320 \times 320 \times 150$
spatial resolution $\Delta_x \times \Delta_y \times \Delta_z$	$3.125 \times 3.125 \times 0.8$ m^3
time step Δ_t	0.4 s
surface heat flux Q_0	150 W m^{-2}
mixed layer depth h	-80 m
convective velocity w_*	1.778×10^{-2} m s^{-1}
eddy turnover time T_*	1.25 h

The flow and temperature fields are solved on a collocated grid in the horizontal direction and a staggered grid in the vertical direction. A pseudospectral method is used in the horizontal direction and a second-order central finite-difference method is used for the vertical derivatives. We use a finite-volume method to solve the Eulerian particle evolution [23]. The scheme is advanced in time using a second-order Adams-Bashforth scheme along with a projection method (by constructing and solving a pressure Poisson equation) to enforce the no-divergence condition. More details of the basic LES solver can be found in Refs. [5,11,16].

B. Simulation setup

We focus on a simplified case of an OML flow in a free-convection scenario. Surface wind stress, Coriolis, and wave effects are not considered and the only forcing is an upward heat flux (ocean cooling) of 150 W m^{-2} at the surface, which is considered moderate for nighttime conditions for midlatitude oceans. It is worth noting that a test case was run including the Coriolis acceleration which produced virtually no difference in the bulk characteristics of the resulting flow (which we attribute to the fact that there is no mean flow, only fast-changing turbulent flow). Given this test result, we proceeded only with the simulation without Coriolis force for simplicity.

Simulations were run on a $320 \times 320 \times 150$ grid spanning $1000 \times 1000 \times 120$ m^3 with a time step of 0.4 s. An initial mixed layer depth $h = -80$ m was imposed at the beginning and was enforced by a two-step temperature gradient in the thermocline characterized by $\partial\langle\tilde{\theta}\rangle/\partial z = 0$, 0.1, and 0.02 K m^{-1} in the ranges $z/h < 0.95$, $0.95 \leqslant z/h \leqslant 1.05$, and $1.05 < z/h$, respectively. The depth of the thermocline was monitored and verified to not change significantly during the statistical sampling period. In all the statistical steady-state results presented, the calculated OML depth (inferred by the location of the negative peak of $\langle w'\theta'\rangle$) was approximately $h \approx -79$ m. We use a sponge layer at the bottom of the domain and a free-slip condition at the top, as well as a no-flux condition for the particle concentration at $z = 0$. Table I presents a summary of the simulation parameters.

In terms of grid convergence we note that simulations that use a Lagrangian scale-dependent dynamic model have been shown to converge at coarser resolutions than simulations using a constant-coefficient Smagorinsky model [24,25]. In the case of Salesky *et al.* [25], who used a modified version of the same code used here, convergence was achieved with $|h|/\Delta_f = 43$ (see the Appendix in Ref. [25]), where $\Delta_f = (\Delta_x \Delta_y \Delta_z)^{1/3}$. In our simulation $|h|/\Delta_f = 40$, which is close enough to the value obtained by Salesky *et al.* [25] so that grid convergence can be safely assumed. It is worth noting that, for highly buoyant particles, the concentration close to the surface decays over a depth shorter than our vertical resolution can resolve. However, resolving this decay is not critical since we are interested mainly in the horizontal patterns of particle concentration for which only the horizontal particle motions need to be well resolved. Since the horizontal velocities are not influenced by w_r, we conclude that the horizontal advection of particles is resolved with enough accuracy.

TABLE II. Particle terminal rise velocities, floatabilities β, and their associated droplet sizes considering oil as the particle. The association with diameter is done within 5 μm of accuracy.

Parameter	C0.00	C0.01	C0.05	C0.19	C0.30	C0.44	C0.59	C0.78	C1.21	C1.75	C3.11
w_r (mm s^{-1})	0	0.216	0.864	3.45	5.40	7.77	10.58	13.82	21.59	31.09	55.27
β	0	0.0121	0.0486	0.194	0.304	0.437	0.595	0.777	1.21	1.75	3.11
equivalent oil droplet diameter (μm)	0	50	100	210	270	340	410	500	710	950	1000

We also note that our previous assumption that inertial effects can be neglected is supported by our estimate of the Stokes number $\mathrm{St}_\Delta \approx 10^{-4}$, which is based on the smallest resolved eddies of the LES. Here the Stokes number is defined as the ratio between the characteristic timescale of the particles to the characteristic timescale of the flow. When obtaining these scales, the flow timescale was estimated using the magnitude of the strain-rate tensor (which is similar to the magnitude of the vorticity vector) and the particle timescale was estimated using Eq. (A5) from Yang *et al.* [16].

The simulation was allowed to spin up for approximately 45 eddy turnover times, after which the flow was verified to be in statistical steady state before the particle concentration field was initialized. Here an eddy turnover time is defined as $T_* = |h|/w_*$. Although rigorously there is no steady state for penetrative convective flows due to the constant entrainment of thermocline water, we found that for the total simulation time the entrainment rate was small enough that steady state could be assumed for statistical analysis as long as the averaging period was not much longer than around four eddy turnover times.

The particle concentration field was initialized with a uniform unit-valued concentration in the OML. We use 11 different particle cases, which are given in Table II, where each simulated case is denoted by CX, where X is the floatability β. Using this nomenclature the cases are C0.00, C0.01, C0.05, C0.19, C0.30, C0.44, C0.59, C0.78, C1.21, C1.75, and C3.11.

Considering practical applications, we connect the particle velocity for each case with oil droplets sizes using the empirical correlations presented in Refs. [26,27], which take into account the fact that both the Reynolds number and the drag coefficient change as the droplet size changes. We take oil as having density $\rho_d \approx 859.87$ kg m^{-3}, thus, in seawater, a higher value of the rise velocity w_r necessarily implies a larger droplet. The droplet sizes are given in Table II up to 5 μm of accuracy for readability purposes (more accurate droplet sizes can be obtained from the rise velocities also presented in Table II). It is worth mentioning that although it is common for oil from spills to have a significant fraction of its mass in droplets with diameter d larger than 1 mm [28,29], droplet C3.11 is already well into a floater regime for our flow configurations, so having extra droplets with higher rise velocity would not impact the results presented here. Thus, the range of our rise velocities does not limit the application of our results for the case of oil spills, making it possible for some of the results presented to be extended to such cases.

After the particle concentration initialization the simulation with the particle concentration field was run for approximately 26 eddy turnover times. We considered the particle distribution to be in statistical steady state after about 20 eddy turnover times (approximately one day) and all steady-state particle-related statistics were computed for the period consisting of approximately the last 4.5 eddy turnover times. It is important to note that the duration of our simulation is within reasonably expected ocean timescales. Since long periods dominated by convection are not uncommon in the ocean [30,31], we believe that our simulation of the flow can be representative of real oceanic conditions.

IV. RESULTS AND DISCUSSION

For the sake of readability we omit the tilde to indicate grid-resolved variables from now on and define the normalized time as $t_* = t/T_*$ with $t_* = 0$ at the moment of particle concentration

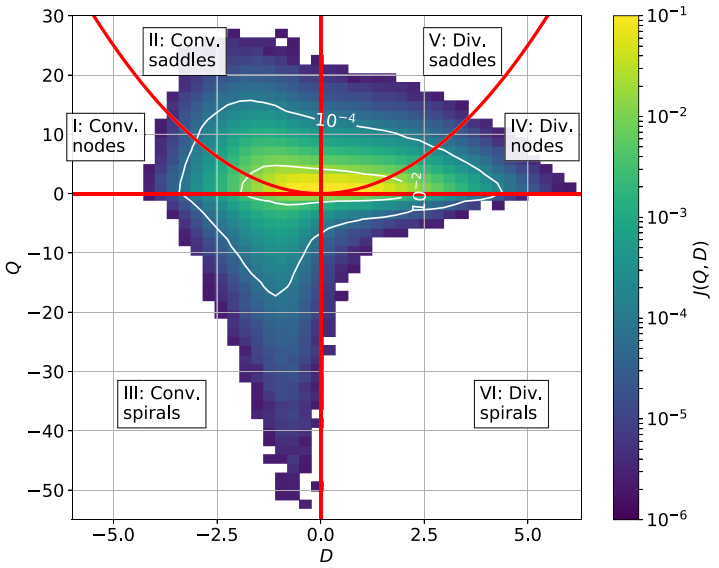

FIG. 2. Joint probability density function of the horizontal divergence D [see Eq. (2)] and the Okubo parameter Q [see Eq. (9)] for the flow field at the surface. The labels in each of the quadrants defined by the red lines are the flow classifications according to Okubo [32].

initialization. We start by first characterizing relevant flow characteristics and then proceed to particle-specific results.

A. Characterization of the flow

In this section we characterize the topology of the surface flow, which will be important when analyzing the horizontal buoyant particles' distribution in steady state. We leave the characterization of statistical variables to the Appendix. In Fig. 2 we show the joint probability density function of the normalized horizontal velocity divergence D and the normalized Okubo parameter Q, defined as [32]

$$Q = \frac{1}{\langle |\boldsymbol{S}|^2 \rangle_{\mathrm{vt}}} \left[\underbrace{\left(\frac{\partial u}{\partial x} - \frac{\partial v}{\partial y} \right)^2}_{\text{stretching}} + \underbrace{\left(\frac{\partial u}{\partial y} + \frac{\partial v}{\partial x} \right)^2}_{\text{shearing}} - \underbrace{\left(\frac{\partial v}{\partial x} - \frac{\partial u}{\partial y} \right)^2}_{\text{vorticity}} \right]_{z=0} \tag{9}$$

for the surface flow in steady state, where only the horizontal components are taken into account. We refer to Q as the Okubo parameter to make the explicit distinction from the Okubo-Weiss parameter [32,33]. The Okubo-Weiss parameter and the Okubo parameter are obtained through the same reasoning and have similar physical meaning and formulation, the main difference being that the Okubo-Weiss parameter is simplified for two-dimensional incompressible flows (following the work of Weiss [33]), which greatly simplifies analyses. We base ourselves only in the work of Okubo [32], which did not make any assumptions about compressibility. We find it appropriate to note at this point that regions of $Q > 0$ can be understood as being strain dominated, while regions of $Q < 0$ are equivalent to vorticity-dominated areas, which we call spirals following the nomenclature of Okubo [32].

The red lines in Fig. 2 are the curves $Q = 0$, $D = 0$, and $Q = D^2$, which define the major flow types according to Okubo [32]: convergent nodes, saddles, and spirals, and divergent nodes, saddles, and spirals as indicated in their respective regions in Fig. 2. We formalize this classification by

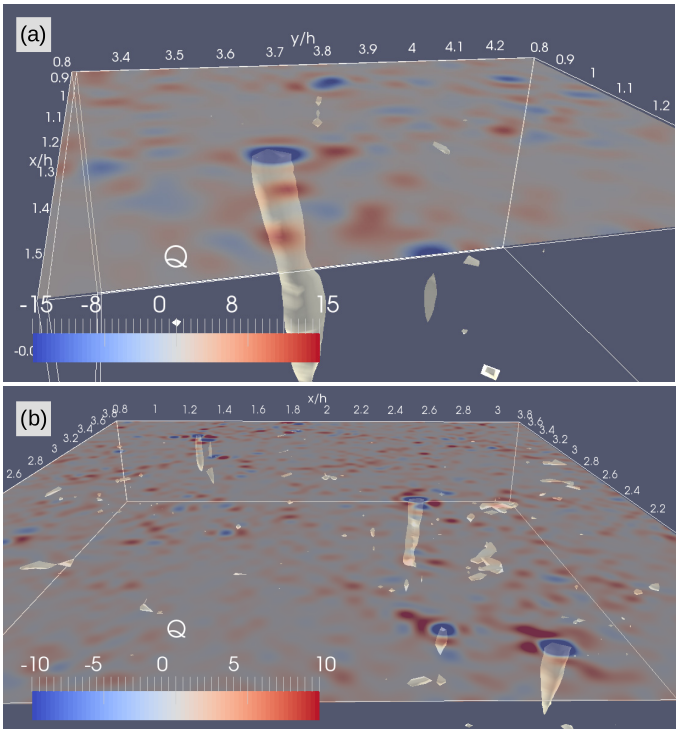

FIG. 3. Detail of (a) a strong vertical vortex and (b) several vertical vortices in a small region of the simulation domain. The color contours shown at the top surface are the 2D Okubo parameter Q and the isosurface is a surface of constant 3D Okubo-Weiss parameter Q_{3D}.

denoting different regions by a set of symbols collectively denoted by P, where P can assume values $P = \text{I,II,}\ldots\text{,VI}$, respectively, depending on the values of D and Q at any given point $\boldsymbol{x}$ and time t. The meaning of I, II, ..., VI is listed in Fig. 2. In his original paper, Okubo [32] presented other classifications that happen when the (Q, D) pair falls exactly on the red lines in Fig. 2. Since this virtually never happens numerically, we omit those from our analysis. More details regarding this classification of points can be obtained in Ref. [32].

When analyzing Fig. 2, it is clear that points that have small values of both Q and D are significantly more common than points in the extreme (note that the color bar is in logarithmic scale). Furthermore, we see that points that are strain dominated ($Q > 0$) have higher probability density than their vorticity-dominated counterparts. Finally, while there are some cases of convergent vorticity-dominated areas (III, convergent spirals), there are significantly fewer cases of divergent vortical regions (VI). This is due to vortex stretching, which amplifies vorticity in the downwelling (convergent) regions and has an opposite effect for upwelling. It is worth noting that convergent regions are colder with respect to their vicinity. This is the case because convection is the only forcing, thus a negative buoyancy anomaly is the general cause for downwelling, which coincides with convergence at the surface.

Furthermore, although convergent spirals are significantly less common than strain-dominated zones, their persistence time is much longer than types of surface flow structures, which was verified to be true for our case by visual inspection (but is a well-known behavior in 2D turbulence [34,35]). This can be understood by noting that the great majority of convergent spirals at the surface (negative peaks in Q) are actually one end of a 3D vortex tube that extends downward from the surface. One example can be seen in Fig. 3(a), in which the surface colormap is the Okubo parameter Q [Eq. (9)]

and the isosurfaces shown are surfaces of constant Q_{3D}. Here Q_{3D} is one of the three-dimensional tensor invariants of the flow [36] normalized by the strain rate

$$Q_{3D} = \frac{1}{\langle |\boldsymbol{S}|^2 \rangle_{vt}} (|\boldsymbol{S}|^2 - |\boldsymbol{\Omega}|^2), \tag{10}$$

where $\boldsymbol{\Omega} = \frac{1}{2}[\nabla \boldsymbol{u} - (\nabla \boldsymbol{u})^T]$ is the rotation tensor. Note that Q_{3D} is the three-dimensional analog of the Okubo [32] parameter Q and it is defined here with the opposite sign as it is generally used in the 3D turbulence literature [36,37] in order to agree with Eq. (9) in a 2D special case. Vortices such as the one in Fig. 3(a) are known to be resilient features in the flow [38,39], in our case often persisting over one eddy turnover time ($T_* = |h|/w_*$), even though their scale is considerably smaller than the mixed layer depth. They are also a common feature at any given time, as can be seen in Fig. 3(b), which shows a small part of the domain with several such examples. Their persistence and frequency of occurrence allows for many vortex merging events, both destructive (when the vortices have opposite-sign circulations) and constructive (when vortices have same-sign circulations). Since negative peaks in Q at the surface are one end of these vortices, they are also persistent (defined here as having a lifetime of roughly an eddy turnover time or larger), have frequent merging events, and, as a consequence, will turn out to have a key effect on surface particle distribution, as will be shown in Sec. IV B.

B. Surface particle distribution

In this section we focus on the horizontal distribution of the particles on the surface, with the goal of understanding the mechanisms that act to produce the structures like the one depicted in Fig. 1, specifically the preferential concentration effects already introduced. The particle initial condition is $C(\boldsymbol{x},t)/C_* = 1$ in every point in the domain that has near-zero-temperature gradient, where C_* is a particle concentration scale. In this simulation this corresponded to having roughly the first 70 m of the OML start with unit normalized concentration. This specific initial condition ensures that particles will be easily mixed in the OML and that the particle distribution will reach statistical steady state within a short period of time.

As previously discussed, Fig. 1 shows the surface concentrations for cases C0.19, C0.44, and C1.21 [Figs. 1(a), 1(b), and 1(c), with floatabilities $\beta = 0.194$, 0.473, and 1.21, respectively], with the divergence D in Fig. 1(d). A closer look at the figure reveals that, while the largest values of the particle concentration field (in all three cases) are concentrated in convergence zones (due to the primary preferential concentration effect), particles with higher buoyancy have a preference for certain parts of the convergent regions as opposed to others (due to the secondary preferential concentration effect). We quantify and explain this by performing a flow topology analysis based on Ref. [32] following the previously mentioned classification of points in types P (see Fig. 2). We first introduce the P-conditioned average particle concentration at the surface, $C_P(P,t_*)$, defined as

$$C_P(P,t_*) = \langle C(\boldsymbol{x},t_*)|P\rangle|_{z=0}, \tag{11}$$

where $P = \mathrm{I},\mathrm{II},\ldots,\mathrm{VI}$ is the flow classification based on [32]. We plot the evolution of C_P (normalized by the average particle concentration at the surface $\langle C\rangle_s$) in Fig. 4 for six different cases (C0.00, C0.19, C0.44, C0.59, C0.78, and C3.11). It is clear that for early times ($t_* \lesssim 0.5$) the immediate general behavior for buoyant particles is for concentrations to rise in convergent regions (I, II, and III) and to decrease in divergent regions (IV, V, and VI). This primary preferential concentration effect was explained in Sec. I as a straightforward consequence of downwelling plumes and that is now being quantified. After this initial behavior, we can see in cases C0.44–C3.11 that the particle concentration in convergent nodes (I) begins to decrease, while the concentration in convergent spirals (III) continues to increase, until they reach equilibrium roughly after $t_* \approx 5$. The decrease in concentration in convergent nodes and increase in convergent spirals (which is more accentuated the larger the floatability β) is caused by the secondary preferential concentration effect.

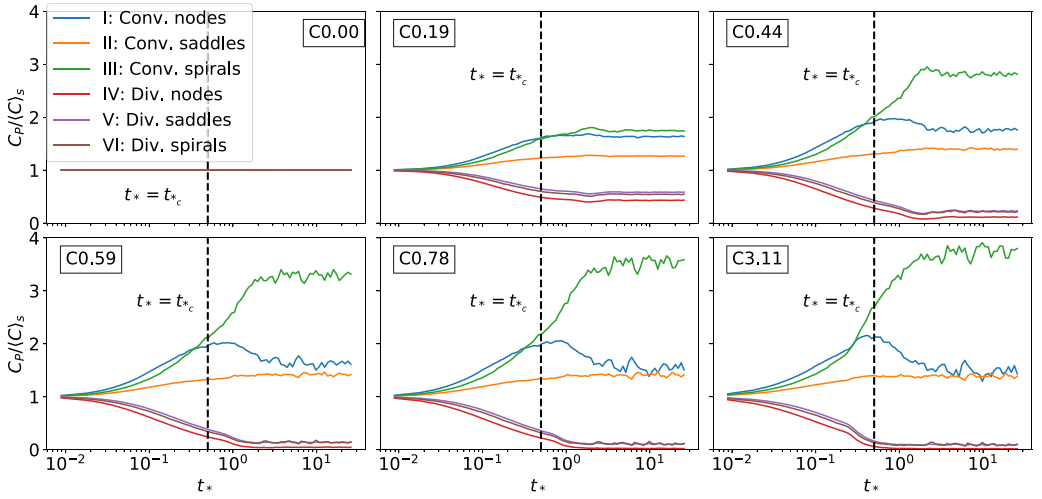

FIG. 4. Time evolution of normalized P-conditioned average particle concentration $C_P(P,t_*)$ for C0.00, C0.19, C0.44, C0.59, C0.78, and C3.11. Here $\langle C\rangle_s$ is the average particle concentration at the surface. Data are smoothed by averaging over logarithmically spaced bins.

Thus, while the primary preferential concentration effect appears immediately after the initial particle release, the secondary effect only becomes evident after a certain time.

Based on this delay for the secondary preferential effect to become apparent, we infer the existence of a critical timescale t_{*_c}, defined as the time at which the secondary preferential concentration mechanism becomes important, and visually estimate it using the curve for the concentration in convergent nodes (I), which shows a very clear inflexion point. In our case we estimate it as roughly $t_{*_c} \approx 0.5$ and mark it in Fig. 4 with vertical dashed lines. Later t_{*_c} is shown to be a consequence of the vortices collecting particles at the surface.

We now plot the equilibrium (steady-state) values as shown in Fig. 4 [which we take as estimates of $C_P(P,t_\infty)$, with t_∞ being an estimate for $t_* \to \infty$] in Fig. 5 as a function of the floatability β. Note that most curves appear to be monotonic with respect to β, with the exception of convergent nodes (I). Despite this exception, the general behavior is clear: The larger the floatability β for a particle, the higher the concentration in convergent spirals (III) in comparison with convergent

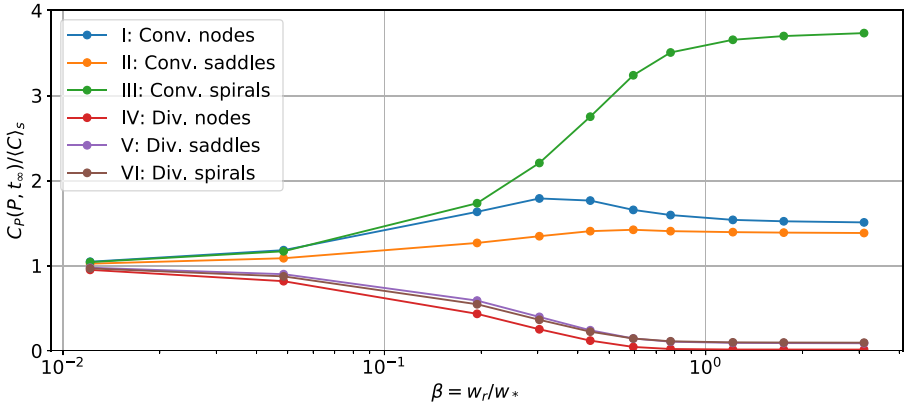

FIG. 5. Steady state for P-conditioned surface concentrations (normalized by average surface concentration) for different types of surface flow structures and different particle cases (plotted as β).

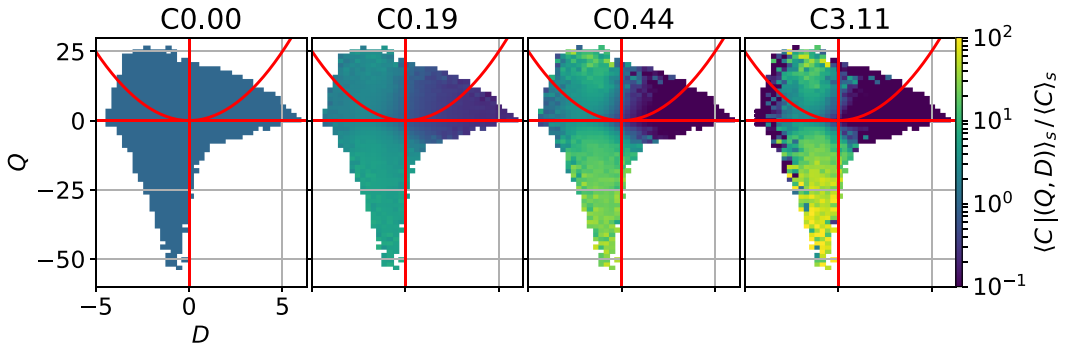

FIG. 6. Concentration map of the conditioned average surface concentration $\langle C|(Q,D)\rangle_s$ normalized by surface concentration for particles C0.00, C0.19, C0.44, and C0.05 in steady state.

nodes (I). Furthermore, as β increases, divergent regions become less and less populated, while the only regions that do not have a significant evolution with β are convergent saddles. Moreover, from Fig. 5 we see that when $0.1 < \beta < 1$ there is a transition behavior from a tracer regime to a floater regime. This is strong indication that the particles in cases C1.21, C1.75, and C3.11 ($\beta \gtrsim 1$) are already in a buoyancy-dominated regime (floaterlike behavior). It is worth noting that, since there are significantly more convergent saddles than convergent spirals in the current convection-driven flow (see Fig. 2), the total masses of particles in regions II and III are very close (not shown), even though region III dominated the magnitude of particle concentration.

A more detailed view of the steady-state regime can be obtained when analyzing the average particle concentration conditioned to (Q,D) pairs, which we denote by $\langle C|(Q,D)\rangle_s$, as shown in Fig. 6 for cases C0.00, C0.19, C0.44, and C3.11. The preference for particles to be concentrated in convergent regions (and "diluted" in divergent regions) is evident for all cases except the nonbuoyant case C0.00, as was expected because of the primary preferential concentration effect. Furthermore, we see that for cases with large β, e.g., C3.11, particles tend to concentrate in the extreme values of $|Q|$. The high concentrations in negative Q peaks can be easily understood, since preference for particles to cluster in convergent spiral regions increases as Q becomes more negative (i.e., the local flow is more dominated by vorticity). Thus, these high concentrations at the bottom of Fig. 6 are another indication of the secondary preferential concentration effect.

The high particle concentrations in regions with positive peaks in Q can be explained only after the mechanism driving the secondary preferential concentration effect is explained. We do that by first noting that strongly vortical convergent regions not only tend to attract particles, but they also have large persistence times (compared to other features of the flow), as was already discussed at the end of Sec. IV A (recall that surface regions with strong negative Q are one end of a vertical vortex). Their effect on tracerlike particles is small, since soon after the particles are attracted to these vortices they are submerged and resurface in divergent regions, which is the reason the secondary preferential concentration effect is not evident for particles in cases C0.00 and C0.19 ($\beta < 0.2$) in Fig. 6. However, particles with large floatability remain on the surface after being attracted to these highly vortical regions, where they get horizontally advected with the vortices themselves (since there is little transfer of particle mass from the vortex to the outside flow) as the vortices collect more particles, thus creating small regions with high concentrations. Hence, vortical regions act as particle collectors and carriers.

This behavior is illustrated in Figs. 7 and 8, which show sequences of snapshots depicting the Okubo parameter Q, particle mass concentration C, and vorticity. The snapshots in both figures advance in time from top to bottom, with an interval between panels of approximately $0.13T_*$ and $0.22T_*$ for Figs. 7 and 8, respectively. In Fig. 7 we see a constructive vortex interaction in which the evolution of the concentration seen in the middle-column panels is dominated by two vortices of

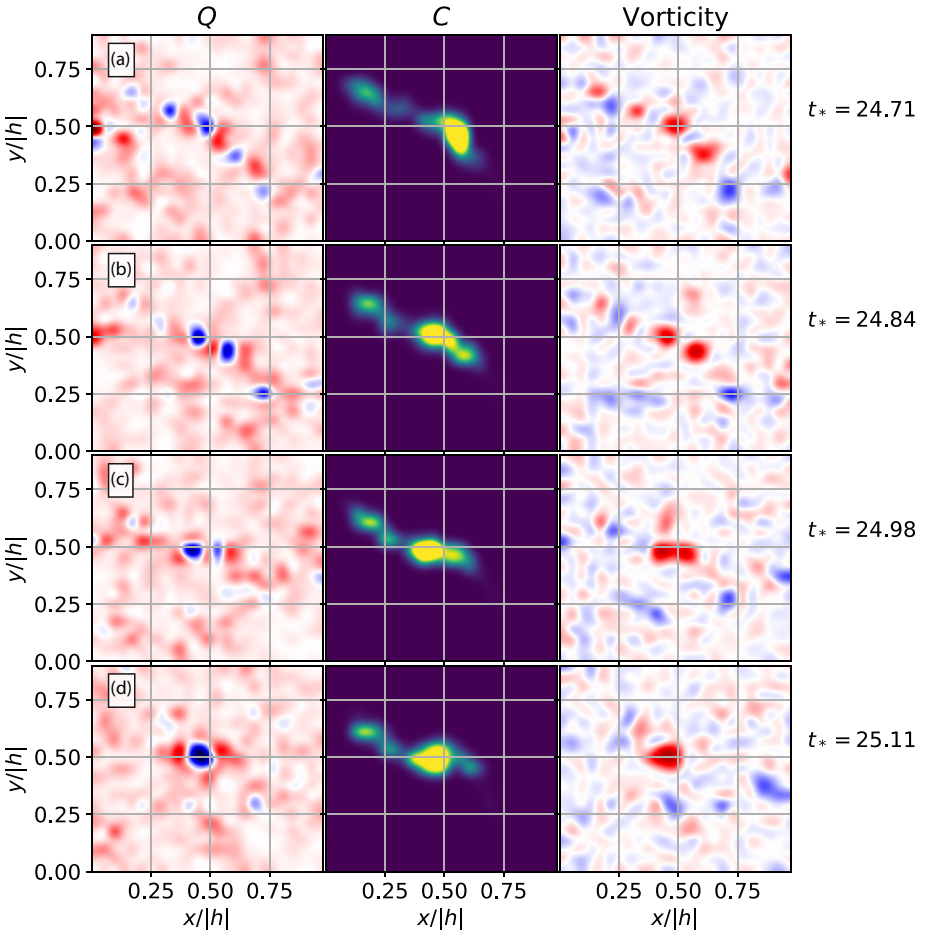

FIG. 7. Sequence of snapshots at increasing time (from top to bottom) of the Okubo parameter Q, particle mass concentration C, and vorticity on the surface. Each set of panels, from (a) to (d), is a different time, which is indicated on the right of the figure. The sequence shows a constructive interaction and the colormaps are the same as in Fig. 1.

positive circulation that interact and merge into a stronger vortex. This type of interaction contributes to produce the peaks in concentration for the strongly negative values of Q shown in Fig. 6. In Fig. 8 we see a destructive vortex interaction in which vortices with opposite-sign circulations weaken each other until finally there is no vortex [Fig. 8(e); see also Supplemental Material [40] for an animated version of this event]. It is also clear in this case that the vortex dynamics completely dominates the high particle concentration region shown in the middle-column panels. Furthermore, this interaction illustrates that destructive mergers leave behind a cluster of "orphan" particles: i.e., particles that were previously inside vortices that were broken apart by the flow.

The vortex interactions just described can also explain the high concentration peaks for large positive values of Q shown in Fig. 6. Notice that positive peaks in Q (which are saddle points and appear as dark red shades in Figs. 7 and 8) are more common at the borders of the vortices that are interacting than anywhere else in the flow. Consider, for example, Figs. 8(a) and 8(b), which show high values of Q (dark red) around the three interacting vortices (dark blue). We see in those figures that while some particles move in between different vortices (which is a process virtually exclusive to interacting vortices), they transition through high-Q regions, which are saddle points with strong straining

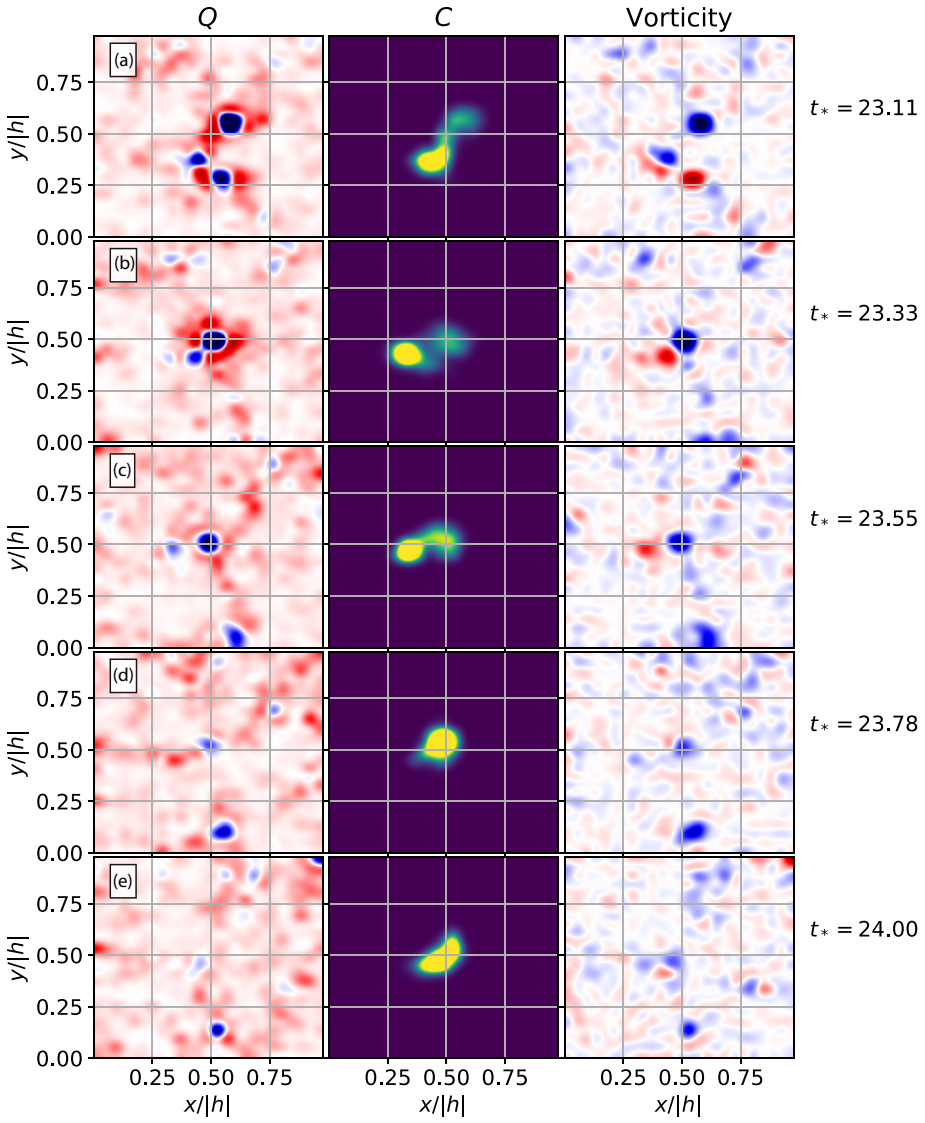

FIG. 8. Sequence of snapshots at increasing time (from top to bottom) of the Okubo parameter Q, particle mass concentration C, and vorticity on the surface. Each set of panels, from (a) to (d), is a different time, which is indicated on the right of the figure. The sequence illustrates a destructive vortex interaction and the colormaps are the same as in Fig. 1.

motion. This suggests that the high particle concentrations in regions with large values of Q shown in Fig. 6 are a consequence of the movement of particles that are caught up in vortex interactions.

These types of vortex interactions (as particle advection mechanisms) are very common and are seen throughout the simulation, thus it is not surprising that they play an important role affecting the surface particle distribution in steady state. As a final remark, we note that they also explain why the secondary preferential concentration effect becomes evident only after some time t_{*_c}. Since the concentration is homogenized in the beginning of the simulation, it takes the flow approximately half of an eddy-turnover time ($t_{*_c} \approx 0.5$) after the initial condition for a significant amount of particles to be collected by the vortices. Before this time, both nodes and spirals (both of which have strong

downwelling motion) attract particles somewhat equally. After t_{*_c} nodes start to break (by straining action of the flow) while spirals persist and continue collecting particles. Thus, the time t_{*_c} is when the persistence of spirals starts to become important so as to make a significant change in the evolution of surface particle concentrations. Note that the vorticity on the surface is likely to concentrate over similar timescales, since the mechanism for horizontal advection acts similarly on both.

V. CONCLUSION

In this work we have studied the mechanisms controlling surface particle distribution in the ocean mixed layer in a free convection regime. A large-eddy simulation was used to simulate the evolution of the particle concentration for 11 different cases with different levels of buoyancy, which translate into 11 different values for the terminal rise velocity, that were assumed to have no inertia.

A primary and a secondary preferential concentration effect were identified and quantified by analyzing the concentration in different surface regions according to a flow topology analysis based on Okubo [32]. We found that the primary preferential concentration effect, in which particles are expelled from horizontally divergent regions on the flow's surface, happens immediately after initialization, as already expected [10]. We also found that the secondary preferential concentration effect, in which particles are attracted to highly vortical convergent regions of the flow, only becomes evident after about 0.5 eddy turnover time and for highly buoyant particles ($\beta \gtrsim 0.5$). This secondary effect was explained as the consequence of resilient surface vortices acting as particles collectors that trap highly buoyant particles in vortical regions. While the particles are trapped, the vortices continue being advected by the flow and collecting more particles until eventually they get weaker and are broken up by the flow. Once again we note that, although the final result is qualitatively similar to preferential concentration of inertial particles (where light particles also concentrate in vortical regions [18]), the mechanism that drives this behavior does not rely on any inertial effects. It is also worth noting that the accumulation mechanism is ultimately the convergence in the convergent spirals and not the vorticity per se. The role of vorticity in the mechanism is to make the convergence last long enough for a significant number of particles to be attracted. Conversely, convergence regions that are not dominated by vorticity are quickly broken up by the flow and have little effect on particle distribution.

Finally, the significant effect of floatability on particle preferential concentration may have important implications for parametrization of subgrid-scale transport in regional and global models. The preferential concentration effects described here (especially the secondary effect) can be understood as antidiffusion, which is a process by which initially separated particles cluster into small regions, instead of spreading out, as time progresses. Antidiffusive behavior of floaters has been observed in larger scales in the ocean, often in connection to spiraling flows [41,42]. Currently, subgrid-scale transport of scalars in regional and global circulation models is parametrized as a diffusive process without any dependence on the buoyancy of the scalar. Although it is hard to assess the impacts that the preferential concentration effects described here may have on larger-scale transport of buoyant particles, it is possible that they are significant enough to make it necessary to include some antidiffusive component linked to a measure of the floatability in the parametrization schemes.

ACKNOWLEDGMENTS

This research was made possible by a grant from the Gulf of Mexico Research Initiative. Data are publicly available through the Gulf of Mexico Research Initiative Information & Data Cooperative [43].

APPENDIX: CHARACTERIZATION OF FLOW STATISTICS

Here we briefly describe the statistical profiles of our simulation, mainly for the sake of completeness. Figure 9 shows some mean flow profiles in steady state. The variance profiles for the horizontal velocities [Fig. 9(a)] have a shape typically expected for free convection, with a maximum

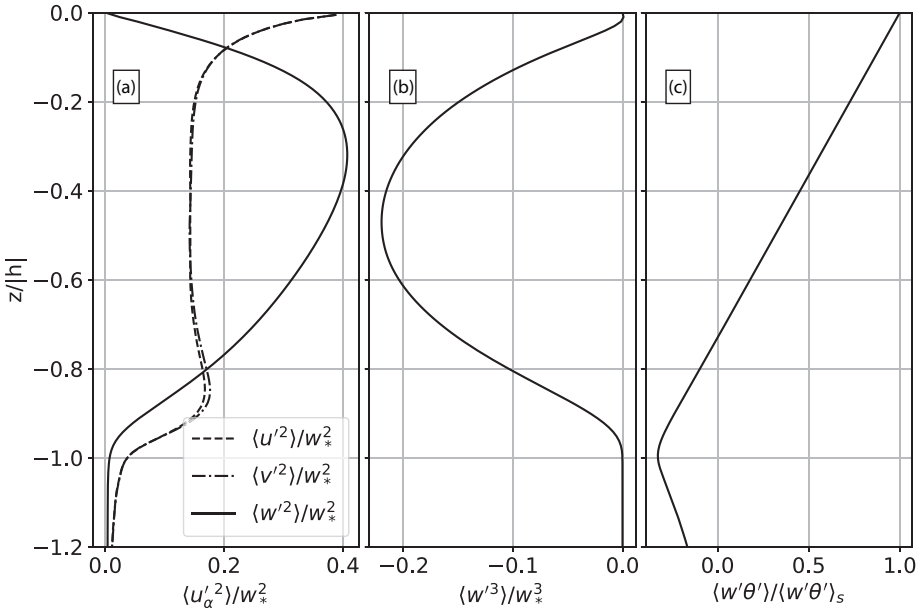

FIG. 9. Profiles of (a) u_α (u, v, and w) variances, (b) vertical velocity skewness, and (c) heat flux for steady state.

at the surface and a smaller peak in the entrainment zone, which is consistent with previous results [44,45]. The variance of the vertical velocity w [Fig. 9(a)] peaks at $z/|h| \approx -0.3$, as is expected [44,45], while its skewness [Fig. 9(b)] peaks at approximately the middle depth of the OML, also in agreement with previous results [45]. The negative values of the skewness, which is an important parameter in boundary-layer dynamics [24], indicate strong downwelling plumes counterbalanced by weak upwelling regions, which we anticipate to have a strong influence on the distribution of the particles in the OML. The heat flux profile [shown in Fig. 9(d)] indicates an upward heat flux that decreases linearly from the surface and has a second (negative) peak in the entrainment layer, consistent with previous results [45].

[1] J. Pedlosky, *Geophysical Fluid Dynamics*, 2nd ed. (Springer, New York, 1987).
[2] T. Kukulka and K. Brunner, Passive buoyant tracers in the ocean surface boundary layer: 1. Influence of equilibrium wind-waves on vertical distributions, J. Geophys. Res.: Oceans **120**, 3837 (2015).
[3] K. Brunner, T. Kukulka, G. Proskurowski, and K. L. Law, Passive buoyant tracers in the ocean surface boundary layer: 2. Observations and simulations of microplastic marine debris, J. Geophys. Res.: Oceans **120**, 7559 (2015).
[4] T. Kukulka, K. L. Law, and G. Proskurowski, Evidence for the influence of surface heat fluxes on turbulent mixing of microplastic marine debris, J. Phys. Oceanogr. **46**, 809 (2016).
[5] D. Yang, M. Chamecki, and C. Meneveau, Inhibition of oil plume dilution in Langmuir ocean circulation, Geophys. Res. Lett. **41**, 1632 (2014).
[6] B. Chen, D. Yang, C. Meneveau, and M. Chamecki, Effects of swell on transport and dispersion of oil plumes within the ocean mixed layer, J. Geophys. Res.: Oceans **121**, 3564 (2016).
[7] J.-H. Liang, J. C. McWilliams, P. P. Sullivan, and B. Baschek, Modeling bubbles and dissolved gases in the ocean, J. Geophys. Res.: Oceans **116**, C03015 (2011).

[8] Y. Noh, I. S. Kang, M. Herold, and S. Raasch, Large eddy simulation of particle settling in the ocean mixed layer, Phys. Fluids **18**, 085109 (2006).
[9] Y. Noh and S. Nakada, Estimation of the particle flux from the convective mixed layer by large eddy simulation, J. Geophys. Res.: Oceans **115**, C05007 (2010).
[10] J. A. Mensa, T. M. Özgökmen, A. C. Poje, and J. Imberger, Material transport in a convective surface mixed layer under weak wind forcing, Ocean Model. **96**, 226 (2015).
[11] D. Yang, B. Chen, M. Chamecki, and C. Meneveau, Oil plumes and dispersion in Langmuir, upper-ocean turbulence: Large-eddy simulations and K-profile parameterization, J. Geophys. Res.: Oceans **120**, 4729 (2015).
[12] T. M. Ozgokmen, A. C. Poje, P. F. Fischer, and A. C. Haza, Large eddy simulations of mixed layer instabilities and sampling strategies, Ocean Model. **39**, 311 (2011).
[13] K. M. Smith, P. E. Hamlington, and B. Fox-Kemper, Effects of submesoscale turbulence on ocean tracers, J. Geophys. Res.: Oceans **121**, 908 (2016).
[14] J. R. Taylor, Accumulation and subduction of buoyant material at submesoscale fronts, J. Phys. Oceanogr. **48**, 1233 (2018).
[15] J. Ferry and S. Balachandar, A fast Eulerian method for disperse two-phase flow, Int. J. Multiphase Flow **27**, 1199 (2001).
[16] D. Yang, B. Chen, S. A. Socolofsky, M. Chamecki, and C. Meneveau, Large-eddy simulation and parameterization of buoyant plume dynamics in stratified flow, J. Fluid Mech. **794**, 798 (2016).
[17] M. R. Maxey, The gravitational settling of aerosol particles in homogeneous turbulence and random flow fields, J. Fluid Mech. **174**, 441 (1987).
[18] J. K. Eaton and J. R. Fessler, Preferential concentration of particles by turbulence, Int. J. Multiphase Flow **20**, 169 (1994).
[19] J. C. Kaimal, J. C. Wyngaard, D. A. Haugen, O. R. Coté, Y. Izumi, S. J. Caughey, and C. J. Readings, Turbulence structure in the convective boundary layer, J. Atmos. Sci. **33**, 2152 (1976).
[20] J. Smagorinsky, General circulation experiments with the primitive equations, Mon. Weather Rev. **91**, 99 (1963).
[21] D. K. Lilly, The Representation of Small-Scale Tubulence in Numerical Simulation Experiments, in *Proceedings of IBM Scientific Computing Symposium on Environmental Sciences*, edited by H. H. Goldstine (Yorktown Heights, New York, 1967), pp. 195–210.
[22] E. Bou-Zeid, C. Meneveau, and M. Parlange, A scale-dependent lagrangian dynamic model for large eddy simulation of complex turbulent flows, Phys. Fluids **17**, 025105 (2005).
[23] M. Chamecki, C. Meneveau, and M. B. Parlange, A hybrid spectral/finite-volume algorithm for large-eddy simulation of scalars in the atmospheric boundary layer, Bound.-Lay. Meteorol. **128**, 473 (2008).
[24] P. P. Sullivan and E. G. Patton, The effect of mesh resolution on convective boundary layer statistics and structures generated by large-eddy simulation, J. Atmos. Sci. **68**, 2395 (2011).
[25] S. T. Salesky, M. Chamecki, and E. Bou-Zeid, On the nature of the transition between roll and cellular organization in the convective boundary layer, Bound.-Lay. Meteorol. **163**, 41 (2017).
[26] L. Zheng and P. D. Yapa, Buoyant velocity of spherical and nonspherical bubbles/droplets, J. Hydraul. Eng. **126**, 852 (2000).
[27] R. Clift, J. R. Grace, and M. E. Weber, *Bubbles, Drops, and Particles* (Dover, New York, 2005), p. 113.
[28] B. Lehr, S. Nristol, and A. Possolo, Deepwater Horizon BP Oil Budget Calculator NOAA report, 2010 (unpublished).
[29] E. E. Adams, S. A. Socolofsky, and M. Boufadel, Comment on "Evolution of the Macondo well blowout: Simulating the effects of the circulation and synthetic dispersants on the subsea oil transport", Environmental Sci. Technol. **47**, 11905 (2013).
[30] K. E. Brainerd and M. C. Gregg, Diurnal restratification and turbulence in the oceanic surface mixed layer: 1. Observations, J. Geophys. Res.: Oceans **98**, 22645 (1993).
[31] W. G. Large, J. C. McWilliams, and S. C. Doney, Oceanic vertical mixing: A review and a model with a nonlocal boundary layer parameterization, Rev. Geophys. **32**, 363 (1994).
[32] A. Okubo, Horizontal dispersion of floatable particles in the vicinity of velocity singularities such as convergences, Deep Sea Res. Oceanogr. Abstracts **17**, 445 (1970).

[33] J. Weiss, The dynamics of enstrophy transfer in two-dimensional hydrodynamics, Physica D **48**, 273 (1991).
[34] P. Perlekar, S. S. Ray, D. Mitra, and R. Pandit, Persistence Problem in Two-Dimensional Fluid Turbulence, Phys. Rev. Lett. **106**, 054501 (2011).
[35] B. Kadoch, D. del-Castillo-Negrete, W. J. T. Bos, and K. Schneider, Lagrangian statistics and flow topology in forced two-dimensional turbulence, Phys. Rev. E **83**, 036314 (2011).
[36] J. Martín, C. Dopazo, and L. Valiño, Dynamics of velocity gradient invariants in turbulence: Restricted euler and linear diffusion models, Phys. Fluids **10**, 2012 (1998).
[37] C. Meneveau, Lagrangian dynamics and models of the velocity gradient tensor in turbulent flows, Annu. Rev. Fluid Mech. **43**, 219 (2011).
[38] G. K. Batchelor, *An Introduction to Fluid Dynamics* (Cambridge University Press, Cambridge, 1973), Sec. 5.3.
[39] P. A. Davidson, *Turbulence: An Introduction for Scientists and Engineers* (Oxford University Press, Oxford, 2004), Sec. 2.3.3.
[40] See Supplemental Material at http://link.aps.org/supplemental/10.1103/PhysRevFluids.3.064501 for an animated version of the event depicted in Fig. 8.
[41] W. Munk, L. Armi, K. Fischer, and F. Zachariasen, Spirals on the sea, Proc. R. Soc. A **456**, 1217 (2000).
[42] E. A. D'Asaro, A. Y. Shcherbina, J. M. Klymak, J. Molemaker, G. Novelli, C. M. Guigand, A. C. Haza, B. K. Haus, E. H. Ryan, G. A. Jacobs, H. S. Huntley, N. J. M. Laxague, S. Chen, F. Judt, J. C. McWilliams, R. Barkan, A. D. Kirwan, Jr., A. C. Poje, and T. M. Özgökmen, Ocean convergence and the dispersion of flotsam, Proc. Natl. Acad. Sci. USA **115**, 1162 (2018).
[43] Available at https://data.gulfresearchinitiative.org/data/R5.x283.000:0002
[44] D. W. Denbo and E. D. Skyllingstad, An ocean large-eddy simulation model with application to deep convection in the Greenland Sea, J. Geophys. Res.: Oceans **101**, 1095 (1996).
[45] D. Wang, Effects of the earth's rotation on convection: Turbulent statistics, scaling laws and Lagrangian diffusion, Dyn. Atmos. Oceans **41**, 103 (2006).